# Impedance Characteristics and Diagnoses of Automotive Lithium-Ion Batteries at 7.5% to 93.0% State of Charge

Qiu-An Huang[a,b,d], Yue Shen[a], Yunhui Huang[a,*], Lei Zhang[c], Jiujun Zhang[c,*]

[a] School of Materials Science and Engineering, Huazhong University of Science and Technology, Wuhan, 430074, PR China
[b] School of Computer Science and Information Engineering, Hubei University, Wuhan, 430062, PR China
[c] Energy, Mining & Environment, National Research Council of Canada, Vancouver, BC V6T 1W5, Canada
[d] Department of Materials Science and Engineering, Pennsylvania State University, University Park, Pennsylvania 16802, United States

## ARTICLE INFO

## ABSTRACT

Diffusion behaviors and reaction kinetics are factors limiting the rate capacity of lithium ion batteries (LIB), particularly in automotive applications. In order to gain a better understanding of the rate-limiting factors of LIBS, a fractional circuit model is constructed and two feedback loops are added to the impedance diagnosis flowchart in this paper. The fractional impedance model is constructed for a commercially available automotive LIB, featured by low internal resistance, long diffusion lengths, and large interfacial areas. Impedance data collected are then used to quantitatively analyze the charge transfer reaction, the status of the solid electrolyte layer (SEI), and the lithium diffusion behavior at different state of charges (SOCs) of $7.5\% \sim 93.0\%$ based on the constructed model and the calculated characteristics frequencies of the corresponding physiochemical processes. The results indicate that both charge transfer resistance and diffusion resistance increased dramatically with decreased SOC values when SOC $\leq 26.5\%$. These results suggest that automotive LIBs should not operate at low SOCs of less than $20.0\%$ or depth of discharging higher than $80.0\%$. Finally, calculations of anode and cathode Warburg impedance percentages offer a simple and quick way to evaluate lithium diffusion abilities through insertion/de-insertion electrodes.

© 2016 Elsevier Ltd. All rights reserved.

## 1. Introduction

Recently, Lithium-ion battery (LIB) technologies are experiencing rapid growth in a number of application areas including portable electronics, stationary power stations and electronic vehicles due to advantages such as salient operation, high energy density, high power density, long cycle-life and environmental friendliness [1,2]. For automotive applications, high capacity and high power LIBs are normally assembled into modules/packages for high-rate operations. Therefore, high-rate capabilities are a prerequisite for LIBs in electric vehicle (EV) applications. The rate capability of LIBs is profoundly dependent on the status of the solid electrolyte interphase (SEI), the insertion/de-insertion reaction and the diffusion behavior [3]. As for the battery management system (BMS) in EV applications, before LIBs are packed into electric vehicles, a quick and substantial diagnosis is required to

ensure qualified performance. This is achieved through the testing of fundamental parameters such as direct current resistance, diffusion behavior, charge transfer reaction, and SEI status [4]. Moreover, above three factors of LIBs are all dependent of state of charge (SOC), so do ultracapacitors [5].

Electrochemical impedance spectroscopy (EIS or AC impedance) is a viable approach that can be used not only in LIBs [6] but also in other electrochemical energy storage and conversion devices, such as fuel cells [7] and ultracapacitors [5,8]. This is due to two main advantages [9,10]: (i) a small signal perturbation guarantees that the cell is not displaced very far from equilibrium during measurements and (ii) the data from a wide-frequency range can be collected with high precision, offering the possibility to separate different physicochemical processes that are overlapping through different characteristic time constants. During the past three decades, many studies of AC impedance have been conducted to investigate SEI statuses, insertion/de-insertion reactions, and diffusion behaviors. For example, Thomas et al. [10] investigated the insertion electrode $Li_{1-x}CoO_2$; Ho et al. [11] studied lithium diffusion in tungsten trioxide thin films; Levi et al. [12] investigated the kinetics of lithium intercalation into $Li_{1-}$

$_x$CoO$_2$; Takeno et al. [13] gave a quick diagnosis of Li-ion battery packs; Wagg et al. [14] investigated the power capabilities of Li-ion batteries; Zhang et al. [15] studied SEI formations; Osaka et al. [16] evaluated a proposed circuit model in which a growing SEI was taken into account for a commercial LIB through fitting error. All of these studies reviewed above were conducted with an AC impedance approach. As mentioned before, lithium diffusion behaviors, kinetics of charge transfer reactions, and status of SEI layers are all important parameters that determine the rate capabilities and power performances of LIBs [3]. For automobile applications, rate capabilities and power performances are critical for successful technology implementation. Therefore, a quick diagnosis for the above parameters at various values of SOC is necessary for battery management systems in order to guarantee the reliability, safety and efficiency of the battery or ultracapacitor modules [1,4,5]. As far as we know, there are a few investigations of the above parameters for LIBs applied in electric vehicles, in particular for automotive LIBs at various SOC values. Electric vehicle LIBs possesses lower internal resistances, longer diffusion lengths, and larger interfacial areas than that of normal LIBs, leading to more prominent inductance effects, larger diffusion time constants, and further deviations from ideal interfaces than that of normal LIBs.

In this paper, we have conducted a quick but substantial diagnosis of automotive LIBs using fractional impedance spectroscopy with an attempt to gain a fundamental understanding of lithium diffusion behaviors, charge transfer reactions and SEI layer statuses at different SOCs. The constructed fractional impedance model takes all of the intrinsic characteristics of automotive LIB into account. These intrinsic characteristics are mainly comprised of constant phase elements representing non-ideal interfaces [17], semi-infinite Warburg impedances representing lithium solid state diffusions [18,19], and inductance representing high-frequency inductance effects. Fractional impedance modeling plays a critical role in LIBs as well as in ultracapacitors [20], hence we discuss this core question in subsequent two sections of "2.1. Fractional impedance elements" and "3.3. Modeling of fractional impedance spectra". Through the impedance diagnosis of LIBs presented in this work, we believe that the method developed here should be considered as the general approach for impedance diagnosis of other devices for electrochemical energy storage and conversion in automotive applications.

## 2. Experimental

### 2.1. Fractional impedance elements

In our approach, traditional resistance $R$ is expressed as impedance ($Z_R = R$), inductance $L$ as $Z_L = j\omega L$, and capacitance $C$

as $Z_C = \frac{1}{j\omega C}$. The distributed or fractional impedance elements are used to simulate the measured impedance spectra in order to obtain simulation results with higher precision. In order to construct better fractional impedance models so as to gain deeper understanding into the reaction kinetics and diffusion behaviors of automotive LIBs, we analyzed and simulated typical fractional impedance elements such as constant phase elements and diffusion impedance elements with parameters closely related to that of an actual Li-ion battery.

#### 2.1.1. Constant phase elements

Capacitance, an interfacial impedance that can be used to characterize properties of the double-layer region of electrodes/electrolytes, can be induced by a non-faradaic process [21]. Normally, a capacitance ($C$) in parallel with a resistance ($R$) produces a semi-circle in a Nyquist plot. However, due to the fraction or roughness of electrode surfaces [17], uneven distribution of reaction rates [22], varying thicknesses or compositions [23], and non-uniform distribution of currents [24], semi-circles are often depressed. Hence, a constant phase element ($CPE$) is put forth to present the depressed semi-circle. The impedance ($Z_{CPE}$) of the $CPE$ is given by the following equation:

$$Z_{CPE} = \frac{1}{Q(j\omega)^\alpha} \tag{1.1}$$

$$\arg \quad (Z_{CPE}) = -\frac{1}{2}\alpha\pi \tag{1.2}$$

where $Q$ is the amplitude, $\alpha$ is the fractional exponent ranging from $-1$ to 1, and $\omega$ is the angular frequency of $CPE$. Obviously, the $\arg(Z_{CPE})$ of $CPE$ is independent of $\omega$, which makes it a valuable property to discern $CPE$. There are four special cases for the exponent factor $\alpha$:

(i) $\alpha = -1.0$, $CPE$ degenerates into $Z_{CPE}|_{\alpha=-1} = j\omega Q^{-1}$, equivalent to a pure inductance $L \triangleq Q^{-1}$;

(ii) $\alpha = 0$, $CPE$ degenerates into $Z_{CPE}|_{\alpha=0} = Q^{-1}$, equivalent to a pure resistance $R \triangleq Q^{-1}$;

(iii) $\alpha = 0.5$, $CPE$ degenerates into $Z_{CPE}|_{\alpha=0.5} = \frac{1}{\sqrt{j\omega}Q}$, equivalent to a semi-infinite diffusion Warburg impedance $Z_{W\infty} = \frac{\sigma}{\sqrt{j\omega}}$, where $\sigma \triangleq Q^{-1}$ is the mass-transfer coefficient or Warburg coefficient;

(iv) $\alpha = 1.0$, $CPE$ degenerates into $Z_{CPE}|_{\alpha=1.0} = \frac{1}{j\omega Q}$, equivalent to a pure capacitance $C \triangleq Q$.
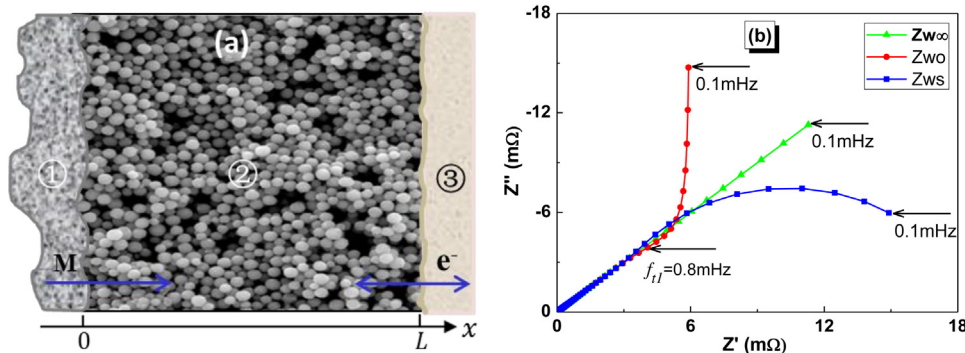


**Fig. 1.** (a) Scheme of the diffusion of redox species M through the porous electrode; (b) Warburg impedance simulation for $Z_{W\infty}$, $Z_{Wo}$ and $Z_{Ws}$ with frequencies ranging from 0.1mHz to 0.1 MHz. Herein, $\sigma = 3*10^{-4} \Omega s^{-\frac{1}{2}}$, $l = 1*10^{-6} m$, $D = 5*10^{-12} cm^2 s$.

### 2.1.2. Diffusion impedance elements

Diffusion-controlled mass transfer of electroactive species, whether in the electrolyte or in the electrode, might result in a Warburg impedance if the diffusion is driven by a gradient in composition and not by an electric field. For the convenience of our discussion, we provided a scheme to show the migration of electroactive species through the electrolyte or the electrode in LIBs (or fuel cells), as shown in Fig. 1a. The diffusion impedance modeling of LIBs still possesses open questions due to its complexity. One instance of this is that it relies on at least three scale structures [25,26] such as the primary particle in submicrons, the secondary agglomerate in several microns, and the porous electrode in hundred microns. The left region marked with ① is the electrolyte; the right region marked with ③ is the current collector, the region sandwiched between ① and ③ is the electrode marked with ②, $L$ is the thickness of the electrode, $M$ is the diffusion reactant, and $e^-$ is the electron with the unit negative charge. If $M$ is a cation, such as $Li^+$ and $H^+$, electrons will flow from the current collector to the insertion electrode; if $M$ is an anion, such as $O^{2-}$, electrons will flow from the electrode to the current collector. For both of these cases, the diffusion impedance originates from the concentration gradient of the reactant $M$ through the porous electrode filled with electrolyte. Fig. 1b depicts the impedance spectra of three typical Warburg elements under different boundary conditions, where $f_{t1} = 0.8 mHz$ is the transition frequency from diffusion control to charge saturation for Warburg impedance $Z_{Wo}$ under reflecting boundary conditions [27]. Different from previous reports [18,19], Fig. 1b is a diffusion impedance simulation that is very close to actual LIBs where the transition frequency is calculated from the diffusion coefficient and the diffusion length. These calculations help us to construct a fractional impedance model more suitable for the automotive LIBs studied in this paper.

For the three cases in Fig. 1b, the concepts of Warburg impedance are as follows:

(i) If species $M$ concentration $C(l,t) = 0$ and $\frac{dC(x,t)}{dx}|_{x=l} = 0$, such as in the transmissive boundary condition (also referred to as the short circuit terminus) [9,28], then the Warburg impedance is named as $Z_{Ws}$, and can be expressed by Eq. (2.1) ∼ Eq. (2.5):

$$Z_{Ws} = R_D \frac{\tanh\left(\sqrt{js}\right)}{\sqrt{js}} \tag{2.1}$$

$$R_D = \frac{\sqrt{2}\sigma l_e}{\sqrt{D}} \tag{2.2}$$

$$s = T_D \omega \tag{2.3}$$

$$T_D = \frac{l_e{}^2}{D} \tag{2.4}$$

$$\sigma = \frac{RT}{n^2 F^2 A \sqrt{2}\sqrt{D}C} \tag{2.5}$$

where $R_D$ is the diffusion resistance, $s$ is the dimensionless frequency, $\omega$ is the radial frequency, $T_D$ is the diffusion-related time constant, $l_e$ is the effective diffusion thickness, $D$ is the effective diffusion coefficient of species $M$, $\sigma$ is the Warburg coefficient, $C$ is the concentration of species M, $A$ is the surface area of the electrode/electrolyte interface, $R$ is the gas constant, $T$ is the absolute temperature, and $n$ is the number of electrons transferred.

- If species $M$ concentration $C(l,t) \neq 0$ and $\frac{dC(x,t)}{dx}|_{x=l} = 0$, such as in the reflecting boundary condition (also referred to as open circuit terminus), the Warburg impedance is named as $Z_{Wo}$ [11,29]:

$$Z_{Wo} = R_D \frac{\coth\left(\sqrt{js}\right)}{\sqrt{js}} \tag{3.1}$$

$$f_{t1} = \frac{3.88D}{2\pi l_e{}^2} \tag{3.2}$$

where $R_D$ and $s$ have the same meaning and expression as defined in $Z_{Ws}$.

- In the limiting case of infinite diffusion lengths ($l \rightarrow \infty$) or very small diffusion coefficient $D$, the two Warburg impedances of $Z_{Ws}$ and $Z_{Wo}$ becomes equal, i.e. $Z_{Ws}|_{l\rightarrow\infty} = Z_{Wo}|_{l\rightarrow\infty}$, and can be

**Table 1**
Test procedure for commercial automotive LIB at various values of SOC.

| Experimental Type | Experimental Description | Data File |
|---|---|---|
| Open Circuit | [20 Sec][default] | Step01[auto] |
| Galvanostatic | [-3.5 A, 10 Hour] [default] | Step02[auto] |
| Potentiostatic | [3 Ref, 1Hour] [default] | Step03[auto] |
| Open Circuit | [3 Hour][default] | Step04[auto] |
| Impedance | [Constant E; 0 OC, 5 mV;Log;100k-0.01 Hz][default] | Step05[auto] |
| Open Circuit | [10 Min][default] | Step06[auto] |
| Impedance | [Constant E; 0 OC, 5 mV;Log;100k-0.01 Hz][default] | Step07[auto] |
| Open Circuit | [10 Min][default] | Step08[auto] |
| Impedance | [Constant E; 0 OC, 5 mV;Log;100k-0.01 Hz][default] | Step09[auto] |
| **RepeatLoop(begin)** | [Repeat Cycles: 9, E-Terminate] | |
| Galvanostatic | [3.5 A, 25 Min][default] | Step11[auto] |
| Open Circuit | [1 Hour][default] | Step12[auto] |
| Impedance | [Constant E; 0 OC, 5 mV; Log; 100k-0.01 Hz][default] | Step13[auto] |
| Open Circuit | [10 Min][default] | Step14[auto] |
| Impedance | [Constant E; 0 OC, 5 mV; Log; 100k-0.01 Hz][default] | Step15[auto] |
| Open Circuit | [10 Min][default] | Step16[auto] |
| Impedance | [Constant E; 0 OC, 5 mV; Log; 100k-0.01 Hz][default] | Step17[auto] |
| **Repeat loop (end)** | [default] | |

further degenerated into a semi-infinite diffusion impedance $Z_{W\infty}$ [30],

$$Z_{W\infty} = \frac{\sqrt{2}\sigma}{\sqrt{j\omega}} \tag{4}$$

In another word, diffusion impedance $Z_{W\infty}$, $Z_{Wo}$ and $Z_{Ws}$ all can be called the Warburg impedance $Z_W$, and they should obey common rules: (i) At high frequencies, the Warburg impedance is smaller since diffusing reactants do not have to move far. At low frequencies, the Warburg impedance is larger since diffusing reactants have to move farther [31]; and (ii) lower frequencies correspond to deeper diffusion into the material. If the material is thin, lower frequencies will penetrate the entire thickness, creating a Finite Length Warburg element $Z_{Wo}$ or $Z_{Ws}$; if the material is thick enough so that the lowest frequencies applied do not fully penetrate the layer, it must be interpreted using the semi-infinite diffusion Warburg element $Z_{W\infty}$ [32].

## 2.2. Experiment measurements

### 2.2.1. Targeted battery and test workstation

The targeted LIB investigated in this paper uses graphite as the negative electrode, Li(Ni$_{1/3}$Mn$_{1/3}$Co$_{1/3}$)O$_2$(NCM) as the positive electrode, and 1.2 M LiPF$_6$ in EC/DMC as the electrolyte. The geometrically active electrode area for the anode or the cathode was ∼50 cm$^2$. This battery had a nominal capacity of 15.5Ah, obtained from the datasheet of the manufacturer HeiFeiGuoXuanHighTech Power Energy Co. Ltd, China. The actual capacity was obtained through measurements involving a low-rate (0.05C) discharging from a fully charged state (4.20 V) to the cut-off voltage (2.80 V) without current interruption. All electrochemical tests were conducted in a Solartron1470-1455 electrochemical workstation.

### 2.2.2. Test procedures

The Solartron1470-1455 electrochemical workstation used can be programmed conveniently. Once test procedures are set in advance, all test actions are conducted in turn automatically. In our present work, 72 test actions were conducted automatically in terms of test procedure as described in Table 1. In the Solartron1470-1455 workstation, there is a friendly user interface for us to configure each experimental step. Herein, we take '3 Ref, 1 Hour' in Table 1 as an example to give a detailed description on potentiostatic experiment as follows, (i) Experimental: applied potential is 3 V vs. reference electrode, herein negative electrode acts as reference electrode, and the total time for the potentiostatic mode is one hour; (ii) Data acquisition: the sampling rate is fixed to one point each second; (iii) Experiment termination: instrument running will quit if current larger than 20A or less than −20A. This kind of programmable method can not only increase the flexibility of the tests but also reduces the researcher's test burden.

## 3. Results and discussion

### 3.1. AC impedance results

The 72-step test actions as described in Table 1 were conducted on an automotive LIB and the corresponding terminal voltages and through currents were recorded. The profiles of the terminal voltage and through current as a function of time are shown in Fig. 2. According to the test procedures listed in Table 1, at each SOC, the impedance spectra in Fig. 2 were measured three times in order to check whether the cell has reached a quasi-static state after a 25-minute charge followed by a one-hour relaxation. As
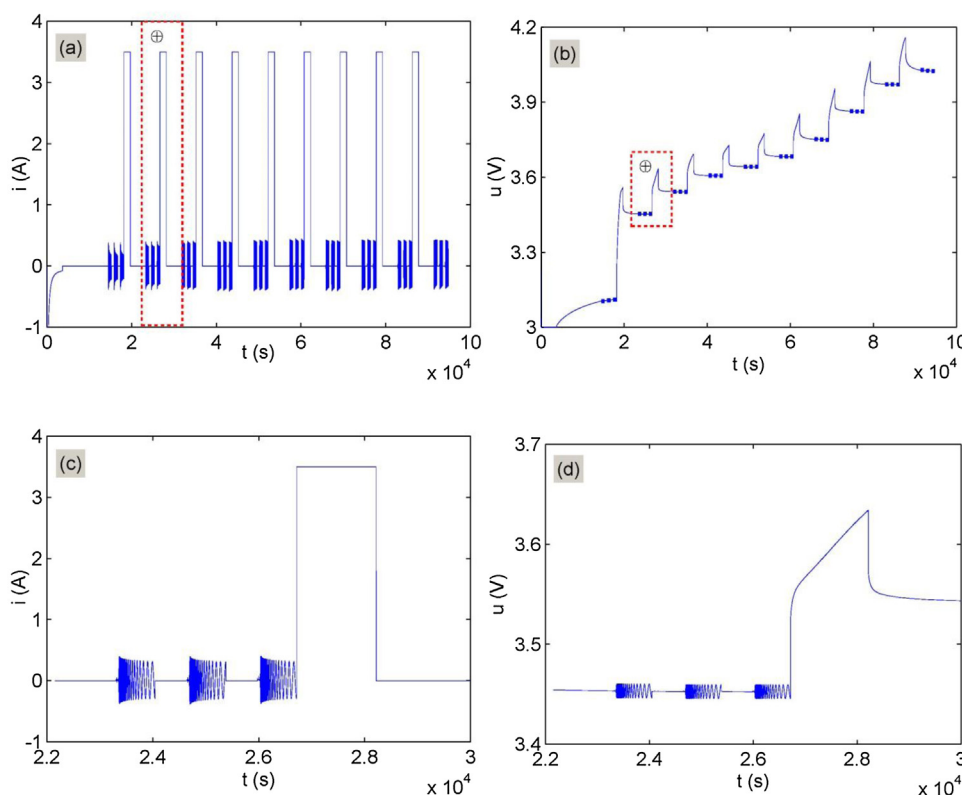


**Fig. 2.** Profiles of through current and terminal voltage for an automotive LIB. (a) Through current; (b) terminal voltage; (c) the enlarged from red block ⊕ inserted in (a); (d) the enlarged from red block ⊕ inserted in (b).
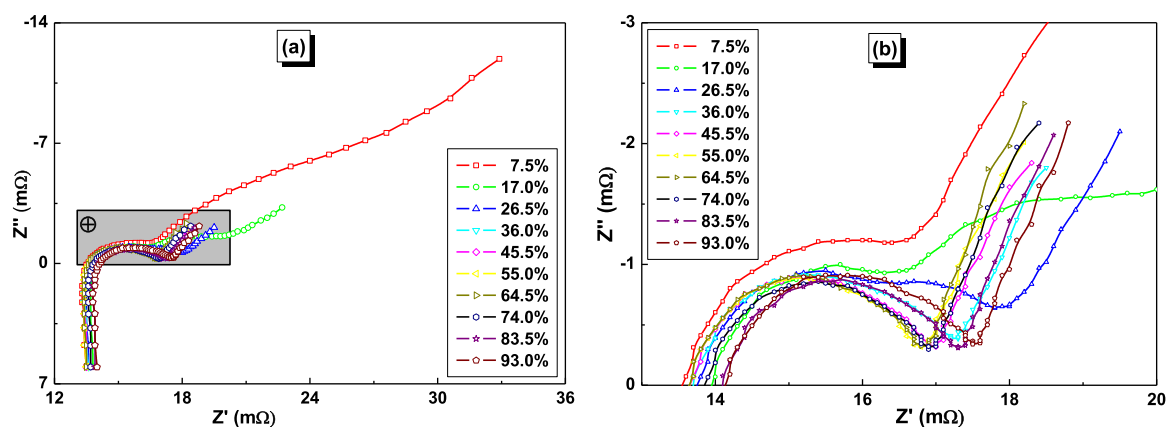
**Fig. 3.** Impedance spectra of the automotive LIB with a rated capacity of 15.4 Ah at SOC values of 7.5% ∼ 93.0%. (a) Impedance plot within the frequency range of 0.01 ∼ 10 kHz; (b) enlarged drawing of impedance spectra from black box marked with ⊕.

observed, the impedance spectra measured at intervals of 10 minutes at each SOC for three times almost completely overlap, suggesting that the cell had approximately reached a stable state. This is the precondition for a quick but substantial diagnosis of the automotive LIB.

Fig. 3 shows the impedance spectra for the battery at various values of SOC in the range of 7.5% ∼ 93.0% with a SOC amplitude of 9.5%.

Two important observations can be seen from Fig. 3: (i) the high frequency intercept on the real axis, which is usually referred to as the ohmic resistance, only shifts a little bit with increasing SOC from 7.5% to 93.0%. This intercept value has other contributing factors besides the ohmic resistance and will be further discussed in a later section of this paper; and (ii) the concentration polarization or diffusion impedance at SOC ≤ 17.0% is much larger than those at SOC ≥ 26.5%, and once SOC is larger than 26.5%, diffusion impedance maintains relatively stable even when SOC continues to increase to 93.0%. Although these diffusion impedance values do not change with the wide-range of values of SOC, contributing factors from different sources should be considered. There should be at least three major factors that can be used to understand the diffusion impedances observed: first, both positive and negative electrodes contribute to the diffusion impedance [31]; second, diffusion impedance relies on both the diffusion coefficient and the concentration of the reactant [9]; third, the diffusion coefficient is not constant but varies with respect to SOC [33].

In addition, the activation polarization loss or resistance has the same evolution trend as that of the diffusion impedance. For a clearer picture of the diffusion behaviors in the automotive LIB, the values of the imaginary part at a fixed frequency of 0.01 Hz from Fig. 3 are detracted and the results obtained are shown in Fig. 4.

Fig. 4 shows that when the SOC increases from 7.5% to 26.5%, the |Z″| value is dramatically decreased from 11.9 mΩ to 2.1 mΩ; a decrease that is greater than 400%, after which the value remains almost constant. This result suggests that when operating a lithium-ion battery module powered electric vehicle, the depth of discharge (DOD) should be less than ∼80%. This is in agreement with previous experimental conclusions between cycling life and DOD [34]. More detailed and deeper diagnosis and analysis for the diffusion behavior and the charge transfer reaction will be discussed in another section.

For clearer observations, Figs. 3 and 4 are combined together into a 3D format, as shown in Fig. 5. The impedance spectra

evolution with respect to SOCs for the targeted automotive LIB are similar to those previously reported [35–38]. However, the transition frequency ($f_{t1}$) is largely perturbed due to the existence of large differences in the diffusion coefficient and the diffusion path length. For example, in our tests, the transition frequency for the targeted battery is less than 0.01 Hz, while the transition frequency was reported to be less than 0.001 Hz by Barsoukov et al. [35], and as large as 1.0 Hz by Ruffo et al. [36]. Different $f_{t1}$ produces different diffusion slope tailors even under the same boundary conditions and with the same frequency ranges of the measurements.

### 3.2. Flow diagram of impedance spectra diagnosis

A diagnostic schematic is helpful to interpret measured impedance spectra. Based on discussions by Orazemand and Huang et al. [7,39], a modified flowchart accounting for the actions of measuring impedance data, modeling, fitting the model, interpreting the results, and optimizing the battery for power generation is presented in Fig. 6. Considering the error analysis of measuring and modeling, two feedback loops are added to the previously reported flowchart [39], as shown in Fig. 6, in which five
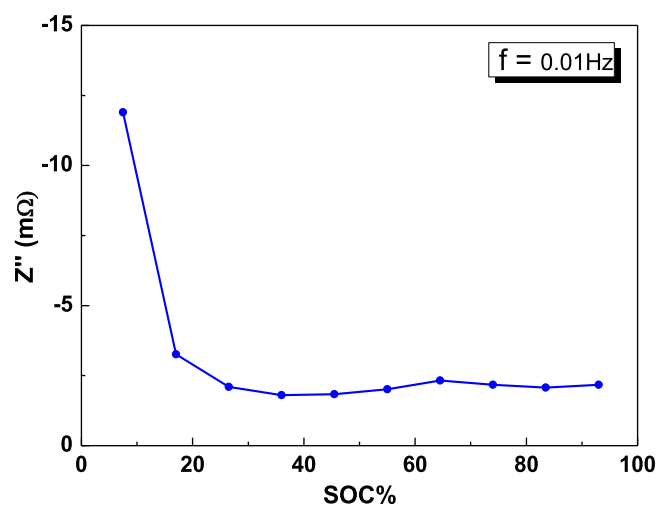


**Fig. 4.** Profile of the imaginary part as a function with SOC values from 7.5% to 93.0% at a fixed frequency of 0.01 Hz for the automotive LIB with a rated capacity of 15.4 Ah.
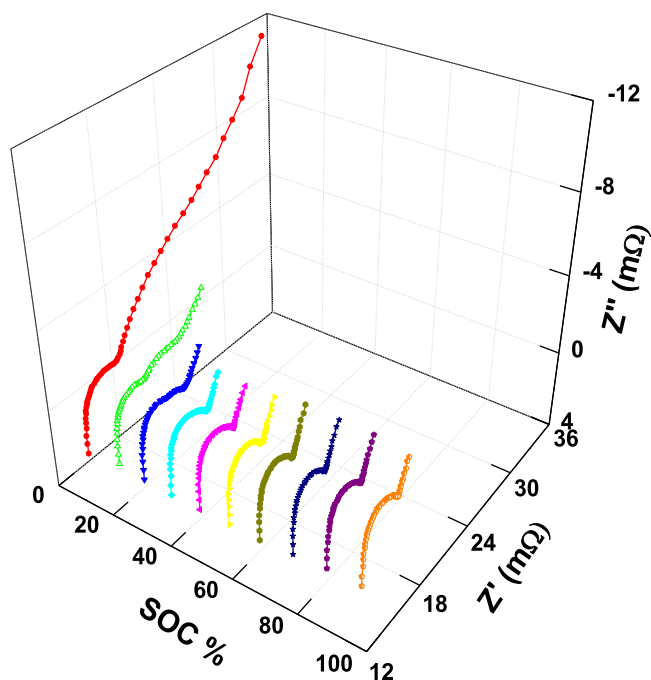
**Fig. 5.** 3D plots of the impedance spectra for the automotive LIB at SOC values of 7.5% ∼ 93.0%.
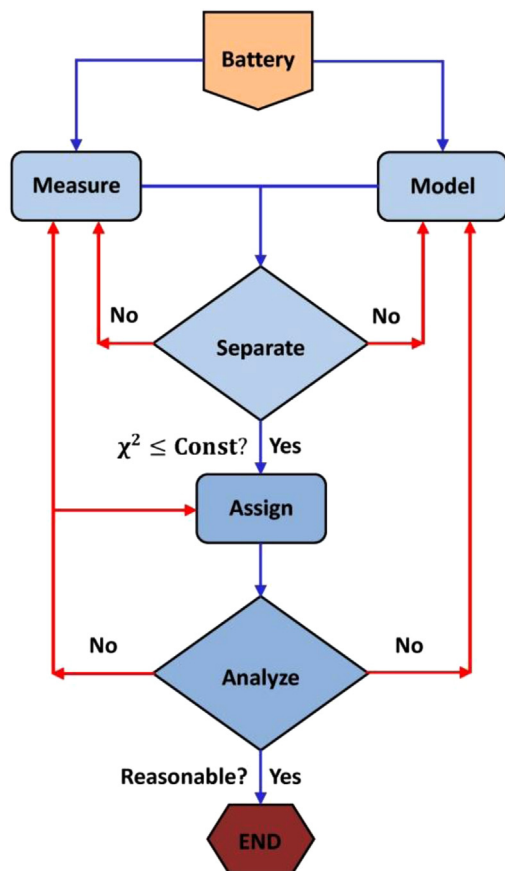


**Fig. 6.** Schematic flowchart of impedance diagnosis showing the relationship between modeling, measuring, separating, assigning, and analyzing with two-level feedback loops.

core steps of measuring, modeling, separating, assigning and analyzing are included and abbreviated as MMSAA, and two-level feedback loops are marked by red arrows.

Two points need to be emphasized in the two-level feedback loops: (i) in the feedback loop of the separating step, the chi-squared function ($\chi^2$) is a good indicatior of the fit quality for the separating step [40]. If $\chi^2 \leq$ Const, whose acutal values rely on noise levels in the measurement and is usually set as $10^{-4}$, diagnosis can go ahead along the blue arrow marked with 'Yes', otherwise it will return to the modeling or measuring step along the red arrow marked with 'No'. And (ii) in the feedback loops of the analyzing step, if the interpretion of the physicochemical phenomena is unreasonable, diagnosis will return to the assigning, modeling or measuring step, otherwise it will end along the blue arrow marked with 'Yes'. In addition to the measurements discussed above, the rest of the four core steps in the flowchart will be addressed in details with an example of the automotive Li-ion battery in our study.

### 3.3. Modeling of fractional impedance spectra

The main focus of this work is to understand the fundamentals governing the diffusion behavior, the charge transfer reaction and the SEI layer status of automotive Li-ion batteries through the analysis of fractional impedance data. In this regard, constructing an equivalent circuit model to describe the processes occurring in a LIB under study is critical. Therefore, prior to constructing/selecting a fractional impedance circuit for this study, typical circuit models used to interpret the measured impedance spectra for LIBs are briefly reviewed as shown in Fig. 7. For the convenience of discussion for equivalent circuit models for LIBs, symbol "∥" denotes in parallel and symbol "⊥" denotes in series for the circuit components. $R_s$ denotes the ohmic resistance of the electrolyte, separator, electrode, and collection, which corresponds approximately to the resistance value at the high frequency intercept of the arc with the real axis (such as those shown in Fig. 3). Generally speaking, there are eight cases involving ten typical equivalent circuit constructions in literature, as shown in Fig. 7.

#### 3.3.1. Case I for the circuit model

$R_s \perp \left( (R_1 \perp Z_{Wo}) \parallel C_1 \right)$, as shown in Fig. 7a. This circuit model contains the least amount of circuit components. In this case, lithium diffusion behaviors were well modeled and deeply investigated under the reflecting boundary conditions assumed [11,41].

#### 3.3.2. Case II for the circuit model

$R_s \perp (R_1 \parallel C_1) \perp ((R_2 \perp Z_{W\infty}) \parallel C_2)$, as shown in Fig. 7b. This circuit model was used to investigate the SEI formation [15], low-temperature effect [42], Ag addition [43], and capacity loss [44] of batteries under semi-infinite diffusion conditions.

#### 3.3.3. Case III for the circuit model

$L \perp R_s \perp (R_1 \parallel C_1) \perp ((R_2 \perp Z_{w\infty}) \parallel C_2)$, as shown in Fig. 7c. This circuit model was used to characterize the cycling life of an automotive Li-ion battery [45]. Compared to Case II, an inductance L is added to represent high-frequency inductance, and the constant phase element CPE took the place of the semi-infinite diffusion Warburg element $Z_{W\infty}$.

#### 3.3.4. Case IV for the circuit model

$R_s \perp (R_1 \parallel CPE_1) \perp ((R_2 \perp CPE_3) \parallel CPE_2)$, as shown in Fig. 7d. This circuit model was used to investigate Lithium diffusion behaviors in graphite electrodes [46]. Compared to Case III, $CPE_1$
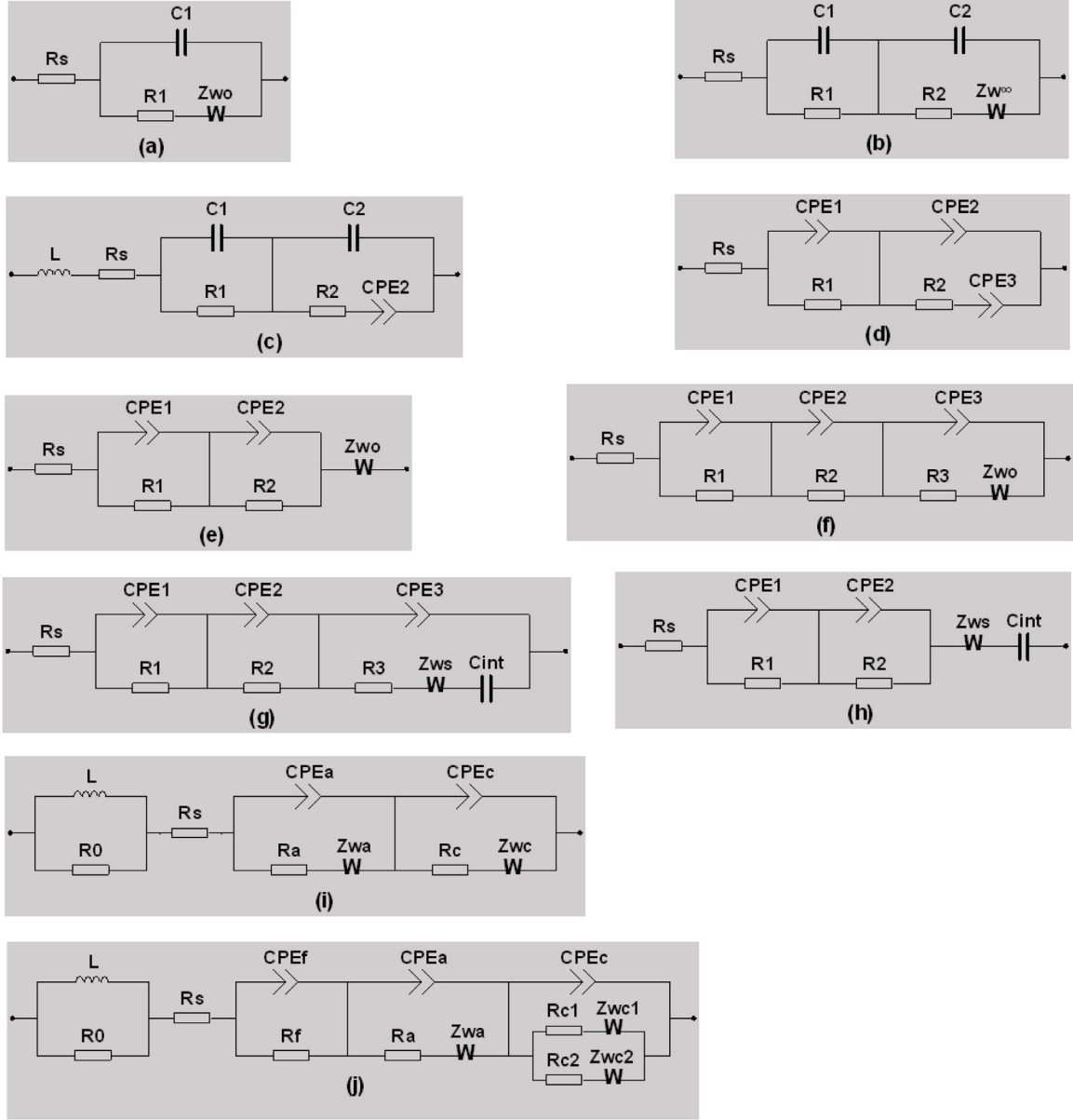
**Fig. 7.** Typical circuit models used to interpret impedance data collected for LIBs from different research groups.

and $CPE_2$ took the places of $C_1$ and $C_2$, respectively, in order to better represent non-ideal interfaces. L was also ignored in this case. Later, Wang et al. [47] simplified the circuit model in Fig. 7d into $R_s \perp (R_1 \parallel CPE_1) \perp (R_2 \parallel CPE_2) \perp Z_{W\infty}$ for the purpose of studying the cycling properties of LIBs.

### 3.3.5. Case V for the circuit model

$R_s \perp (R_1 \parallel CPE_1) \perp (R_2 \perp CPE_2) \perp Z_{Wo}$, as shown in Fig. 7e. This circuit model was used to understand Lithium diffusion kinetics in a single phase $V_2O_5$ [48]. Compared to Case IV, a reflective diffusion Warburg element $Z_{Wo}$ took the place of the constant phase element

**Table 2**
Typical fractional circuit models applied in LIBs.

| Cases | Model Description | Applications |
|---|---|---|
| I: Fig. 7a | $R_s \perp ((R_1 \perp Z_{Wo}) \parallel C_1)$ | [11,41] |
| II: Fig. 7b | $R_s \perp (R_1 \parallel C_1) \perp ((R_2 \perp Z_{W\infty}) \parallel C_2)$ | [15,42–44] |
| III: Fig. 7c | $L \perp R_s \perp (R_1 \parallel C_1) \perp ((R_2 \perp Z_{w\infty}) \parallel C_2)$ | [45] |
| IV: Fig. 7d | $R_s \perp (R_1 \parallel CPE_1) \perp ((R_2 \perp CPE_3) \parallel CPE_2)$ | [46,47] |
| V: Fig. 7e | $R_s \perp (R_1 \parallel CPE_1) \perp (R_2 \perp CPE_2) \perp Z_{Wo}$ | [48] |
| VI: Fig. 7f | $R_s \perp (R_1 \parallel CPE_1) \perp (R_2 \parallel CPE_2) \perp ((R_3 \perp Z_{Wo}) \parallel CPE_3)$ | [49] |
| VI: Fig. 7g | $R_s \perp (R_1 \parallel CPE_1) \perp (R_2 \parallel CPE_2) \perp ((R_3 \perp Z_{Ws} \perp C_{int}) \parallel CPE_3)$ | [49] |
| VII: Fig. 7h | $R_s \perp (R_1 \parallel CPE_1) \perp (R_2 \perp CPE_2) \perp Z_{Ws} \perp C_{int}$ | [51,52] |
| VIII: Fig. 7i | $(R_0 \parallel L) \perp R_s \perp ((R_a \perp Z_{Wa}) \parallel CPE_a) \perp ((R_c \perp Z_{Wc}) \parallel CPE_c)$ | [6] |
| VIII: Fig. 7j | $(R_0 \parallel L) \perp R_s \perp (R_f \parallel CPE_f) \perp ((R_a \perp Z_{Wa}) \parallel CPE_a) \perp ((R_{c1} \perp Z_{Wc1}) \parallel (R_{c2} \perp Z_{Wc2}) \parallel CPE_c)$ | [6] |

CPE$_3$. In addition, $Z_{Wo}$ was removed outside from $R_2 \parallel CPE_2$ for simplification. One thing to note here is that the reported low-frequency impedance tail is not entered from the diffusion-control range into the charge saturation range [48]. Therefore, under this situation $Z_{Wo}$ can be approximated by CPE.

### 3.3.6. Case VI for the circuit model

$R_s \perp (R_1 \parallel CPE_1) \perp (R_2 \parallel CPE_2) \perp ((R_3 \perp Z_{Wo}) \parallel CPE_3)$,as shown in Fig. 7f, or the simplified version $R_b \perp (R_1 \parallel CPE_1) \perp (R_2 \perp CPE_2) \perp (R_3 \parallel CPE_3) \perp Z_{Wo}$.Levi et al. [49] suggested that $Z_{Ws} \perp C_{int}$ was sometimes a better choice than $Z_{Wo}$ to represent Lithium diffusion in electrodes with special thicknesses, as shown in Fig. 7g. Moss et al. [50] later removed $C_{int}$ outside from $(R_3 \perp Z_{Ws} \perp C_{int}) \parallel CPE_3$ and used this modified circuit model to study the dynamic response of LIBs.

### 3.3.7. Case VII for the circuit model

$R_s \perp (R_1 \parallel CPE_1) \perp (R_2 \perp CPE_2) \perp Z_{Ws} \perp C_{int}$, as shown in Fig. 7h. This circuit model was regarded as a simplification of the circuit model in Fig. 7g. By removing the whole $Z_{Ws} \perp C_{int}$ outside from $(R_3 \perp Z_{Ws} \perp C_{int}) \parallel CPE_3$ [47], the circuit model was used to investigate the doping effects [51] and the diffusion behaviors [52] for LIB.

### 3.3.8. Case VIII for the circuit model

$(R_0 \parallel L) \perp R_s \perp ((R_a \perp Z_{Wa}) \parallel CPE_a) \perp ((R_c \perp Z_{Wc}) \parallel CPE_c)$, as shown in Fig. 7i. This circuit model was used to investigate the capacity fade. The charge transfer reaction and the diffusion behavior within both the cathode and the anode are considered simultaneously. $(R_a \perp Z_{Wa}) \parallel CPE_a$ and $(R_c \perp Z_{Wc}) \parallel CPE_c$ [6] both correspond to the randle-like circuit. If both SEI status and particle size factors of the cathode were considered, an improved circuit model is constructed, as shown in Fig. 7j.

Herein, we capsulate fractional circuit models reviewed above into Table 2 for better readability.

From the above discussions concerning circuit models used in literature for LIBs, three conclusions can be made: first, $Z_{Wo}$, $Z_{Ws}$, $Z_{W\infty}$, and CPE can be used to simulate Lithium diffusion behaviors under different boundary conditions, and all of these diffusion impedance elements can be removed outside from the coupled charge transfer reaction process via a circuit simplification or an approximation. Second, constant phase elements can take the place of capacitances if a non-ideal interface is taken into consideration. Third, intercalation capacitance $C_{int}$ is used to simulate charge accumulation effects in insertion/de-insertion electrodes.

In regard to the automotive LIB in this study, a fractional circuit model is constructed based on the following four factors. First, the thickness of the electrodes for the automotive LIB in this study is more than 60 μm, which can lead to a low transition frequency $f_{t2}$ (will be discussed later) and can result in the possibility of the measured low-frequency tailor being located in the diffusion-control region rather than the charge saturation region. Under this situation, $Z_{W\infty}$, $Z_{Wo}$, and $Z_{Ws}$ all behave equivalently and the simplest format of $Z_{W\infty}$ can be used for this study. Second, the larger the interface area at the electrode/electrolyte, the higher the possibility that the interface surface could deviate from the homogeneity. In this case, a constant phase element should be adopted instead of a pure capacitance due to the large interfacial area of the battery under study. Third, the high frequency inductance becomes more prominent due to the lower internal resistance of the high-power LIB. Hence, the inductance becomes critical in this study. Fourth, intercalation capacitance is adopted in order to simulate the charge accumulation effect in the insertion/de-insertion electrode for low-frequency perturbations.

Fig. 8a is the constructed fractional circuit model and the corresponding impedance simulation for the targeted LIB in this study. $Z_{W\infty}$ is defined in Eq. (4), and $CPE_1/CPE_2$ are defined in Eq. (5). L describes the high-frequency inductance, $R_s$ denotes the sum ohmic resistance of the electrode, electrolyte, separator, and connection, $R_1$ in parallel with $CPE_1$ simulates $Li^+$ diffusion through the SEI layer, $R_2$ in parallel with $CPE_2$ simulates $Li^+$ charge transfer reaction at the electrode/electrolyte interface; $Z_{W\infty}$ simulates $Li^+$ diffusion in the porous electrode under semi-infinite diffusion conditions, $C_{int}$ describes the Li-ion accumulation effect in intercalation/de-intercalation electrodes for low-frequency perturbations.

$$Z_{CPE1} = \frac{1}{Q_1(j\omega)^{\alpha_1}}, \text{ and } Z_{CPE2} = \frac{1}{Q_2(j\omega)^{\alpha_2}} \quad (5)$$

Fig. 8b shows an obvious trend where the high frequency X-axis intercept of the depressed semicircle increases with decreasing fractional exponent $a$ even under conditions of fixed ohmic resistance $R_s$. At the same time, inductance L also affects the high frequency intercept. These phenomena indicate that the high frequency intercept is not equal to the ohmic resistance $R_s$ due to the existence of inductance and constant phase elements, in particular for automotive LIBs due to its low internal resistance.

In Fig. 8b, $f_1$ and $f_2$ are the characteristic frequencies for $R_1 \parallel CPE_1$ and $R_2 \parallel CPE_2$, respectively, and $f_{t2}$ is the transition frequency from the kinetic control to the diffusion control. $f_1$ and $f_2$ is the
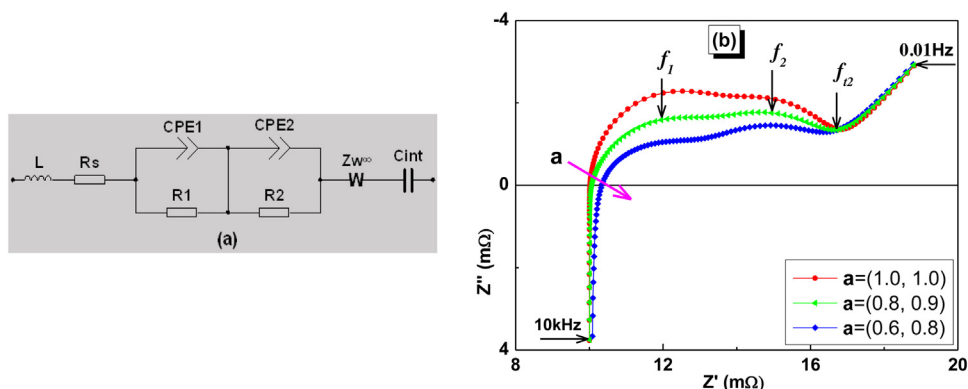


**Fig. 8.** Equivalent circuit model and its corresponding impedance simulation for LIB. (a) A fractional impedance model, and (b) impedance simulation from 0.01 Hz to 10 kHz under conditions of different fractional exponent $a \overset{\underline{def}}{=} (a_1, a_2)$ for $CPE_1$ and $CPE_2$. Herein, $L = 6 * 10^{-8}H$, $R_b = 10^{-2}\Omega$, $Q_2 = 100S \cdot s^{a_1}$, $R_1 = 3.5 * 10^{-3}\Omega$, $R_2 = 2.5 * 10^{-3}\Omega$, and $C_{int} = 5 * 10^5 F$. $f_1$ and $f_2$ are the characteristic frequencies for $R_1 \parallel CPE_1$ and $R_2 \parallel CPE_2$, respectively, and $f_{t2}$ is the transition frequency from kinetic to diffusion controls.
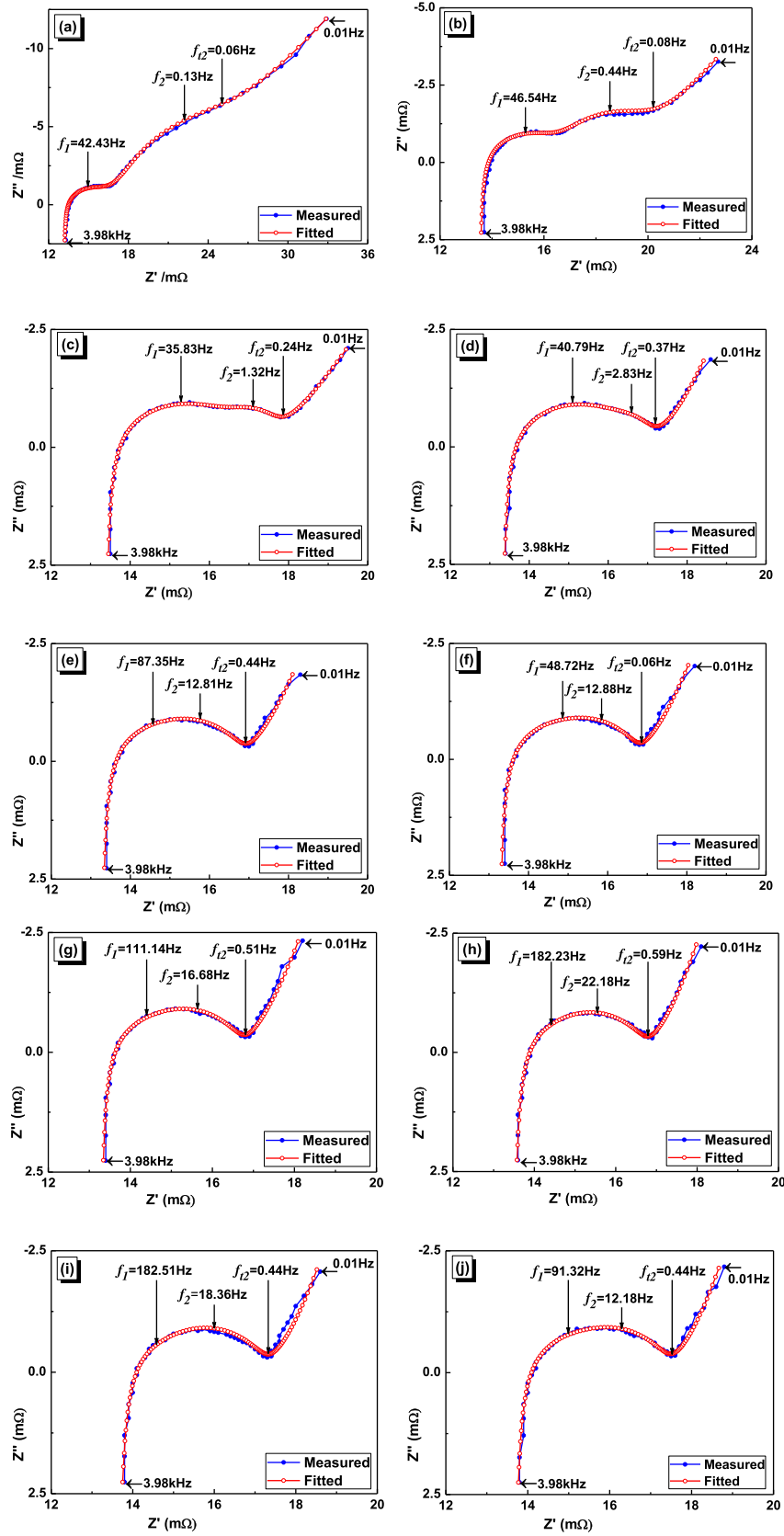
**Fig. 9.** Measured and fitted impedance spectra for the automotive LIB at various values of SOC: (a) 7.5%; (b) 17.0%; (c) 26.5%; (d) 36.0%; (e) 45.5%; (f) 55.0%; (g) 64.5%; (h) 74.0%; (i) 83.5%; (j) 93.0%. Impedance data as shown in Fig. 5 were fitted to the circuit model (Fig. 8a), $f_1, f_2$, and $f_{t2}$ have the same definition as in Fig. 8.

characteristic frequency at which the imaginary part of the impedance reaches the minimum, and the transition frequency $f_{t2}$ corresponds to the local minimum from kinetic to diffusion controls. Moreover, $f_1$ and $f_2$ can be calculated out through Eq. (6) [53]:

$$f_1 = \frac{1}{2\pi(R_1Q_1)^{1/\alpha_1}} \tag{6.1}$$

$$f_2 = \frac{1}{2\pi(R_2Q_2)^{1/\alpha_2}} \tag{6.2}$$

The equivalent capacitances for CPE$_1$ and CPE$_2$ can also be calculated out through Eq. (7) [53]:

$$C_1 = Q_1^{\frac{1}{\alpha_1}} * R_1^{\frac{1-\alpha_1}{\alpha_1}} \tag{7.1}$$

$$C_2 = Q_2^{\frac{1}{\alpha_2}} * R_2^{\frac{1-\alpha_2}{\alpha_2}} \tag{7.2}$$

### 3.4. Separating of the fractional impedance spectra

#### 3.4.1. Fitting processes
Arcs of the impedance spectra recorded for LIBs typically overlap in frequency domain. Separation via complex nonlinear least square fitting is a necessary step to interpret the collected impedance data. Fig. 9 shows both the measured impedance spectra at various values of SOC for the automotive LIB, and the fitted ones using the fractional impedance model in Fig. 8a. Characteristic frequencies($f_1$ and $f_2$), transition frequencies ($f_{t2}$), and a fitting range from 0.01 Hz to 3.98kz are all labeled in Fig. 9. The fitting error and fitted results will be discussed subsequently.

#### 3.4.2. Fitting error
As introduced in the section above, the chi-squared function ($\chi^2$) is an index to assess the fitting quality of the separating step. If the chi-squared function $\chi^2 \geq Const$ (Const relies on the measurement noise level), a bad fit occurs due to either inapproriate model adoption or incorrect impedance data collected. In this situation, the diagnosis has to be turned back to the model/measure step along the first-level feedback loop colored in red, as shown in Fig. 6. In the fitting as shown in Fig. 9, the chi-squared function $\chi^2$ at various SOC values are below or very close to $10^{-4}$, as shown in
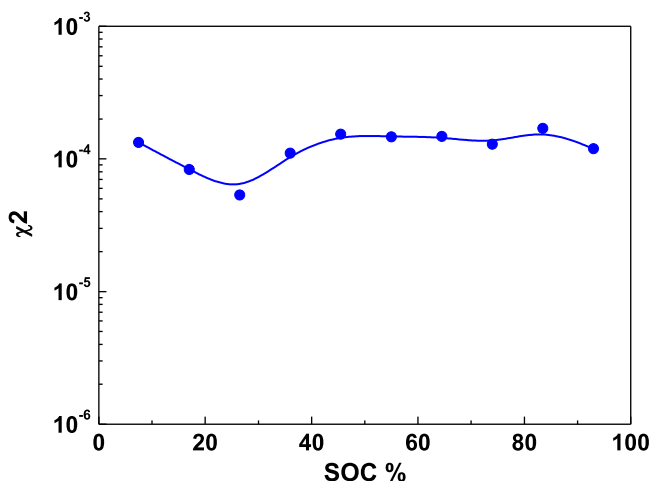


**Fig. 10.** Chi-squared function values at various SOCs of the automotive LIB.

Fig. 10. Hence, the fit or separation in this study is feasible for automotive LIB [40]. In other words, the fitting error is in the tolerable range and the diagnosis can go ahead along the blue route as shown in Fig. 6.

#### 3.4.3. Fitting parameters
Table 3 lists the fitted parameters according to the equivalent circuit model in Fig. 8a. Based on the fitted results, the inductance relative perturbance and ohmic relative perturbation at various SOC values can be calculated based on Eq. (8.1) and Eq. (8.2),

$$\Delta L\% = L - \frac{\overline{L}}{L} * 100\% \tag{8.1}$$

$$\Delta R_s\% = \frac{R_s - \overline{R}_s}{\overline{R}_s} * 100\% \tag{8.2}$$

where $\overline{L}$ and $\overline{R}_s$ are the average values of $L$ and $R_s$ at SOC values of $7.5\% \sim 93.0\%$, as listed in Table 3. $L$ and its relative perturbation $\Delta L\%$ with respect to SOC values from 7.5% to 93.0% are shown in Fig. 11a. $L$ perturbs below 2.0% over SOC values from 7.5% to 93.0%, and hence $L$ is almost indepentant of SOC. At the same time Fig. 11b shows that the changing trend of $R_s$ with respect to SOC is the same as $L$. As a result, Fig. 11 suggests that both the measuring and the separating for the LIB are stable, reliable, and highly accurate.

One point that needs to be emphasized is that a refinement fit between the simulated and measured impedance spectra from the above efforts is not a sufficient condition to validate the theoretical model but rather, a pre-requisite. Therefore, in addition to the fit chi-squared function ($\chi^2$) of the complex nonlinear square-least, other independent evidences are required to validate the theoretical model [49].

### 3.5. Assignment of the fractional impedance spectra

#### 3.5.1. Frequency range in literature
In regard to Li-ion batteries, Levi et al. [12] proposed at least six different sub-processes that might produce impedance spectra. However, one or more impedance arcs or tailor might disappear and/or be indistinguishable under given measurement conditions like SOC (or lithium content), cycle number, temperature, and frequency range [55]. In this study, focus is given to three sub-processes that dominate a LIB's rate capabilities for electric vehicle applications. These three sub-processes produce impedance spectra that are completely distinguishable at 7.5% to 93.0% SOC, which are then analyzed. Table 4 lists typical frequency ranges. As can be seen from Table 4, the frequency ranges for certain sub-processes are different due to the differences in fabrication conditions and electrode compositions/microstructures. However, the relative positions and band widths of the impedance arcs or tails are usually consistent with each other in the frequency domain.

#### 3.5.2. Characteristic frequencies
From the perspective embodied in Fig. 6, the impedance diagnosis in this study is not to demonstrate refinement fit with the smallest number of circuit elements [39], but rather to understand the fundamentals governing SEI layer status, charge transfer reaction, and diffusion behavior in LIBs for battery management systems. A consecutive step after separating is to assign the fitted circuit parameters to certain physicochemical processes. Generally speaking, the characteristic frequency or relaxation time of the LIB remains basically independent of external loads. In other words, the characteristic frequency or relaxation time keeps relatively stable once the cell is fabricated if

**Table 3**
Fitted parameters of the circuit model in Fig. 7a for the automotive Li-ion battery.

| Parameter | SOC | | | | | | | | | |
|---|---|---|---|---|---|---|---|---|---|---|
| | 7.5% | 17.0% | 26.5% | 36.0% | 45.5% | 55.0% | 64.5% | 74.0% | 83.5% | 93.0% |
| $L\left(10^{-8}H\right)$ | 9.85 | 9.84 | 9.83 | 9.84 | 9.84 | 9.78 | 9.77 | 9.85 | 9.99 | 9.89 |
| $R_s(m\Omega)$ | 13.06 | 13.42 | 13.27 | 13.22 | 13.17 | 13.18 | 13.19 | 13.39 | 13.51 | 13.57 |
| $R_1(m\Omega)$ | 5.04 | 2.72 | 0.59 | 0.30 | 1.30 | 1.13 | 1.43 | 1.80 | 1.92 | 1.24 |
| $Q_1(S \cdot s^{\alpha_1})$ | 234.1 | 167.0 | 200.5 | 187.3 | 28.8 | 27.4 | 19.7 | 15.8 | 16.8 | 27.9 |
| $\alpha_1$ | 0.90 | 0.79 | 1.00 | 1.00 | 0.75 | 0.80 | 0.77 | 0.72 | 0.73 | 0.78 |
| $R_2(m\Omega)$ | 3.51 | 3.38 | 3.78 | 3.65 | 2.38 | 2.42 | 2.07 | 1.54 | 1.83 | 2.61 |
| $Q_2(S \cdot s^{\alpha_2})$ | 10.2 | 10.8 | 13.1 | 11.5 | 11.0 | 8.7 | 9.5 | 11.8 | 12.0 | 10.4 |
| $\alpha_2$ | 0.60 | 0.58 | 0.55 | 0.57 | 0.58 | 0.61 | 0.60 | 0.57 | 0.54 | 0.57 |
| $\sigma(m\Omega \cdot s^{-0.5})$ | 4.03 | 1.12 | 0.65 | 0.45 | 0.45 | 0.47 | 0.50 | 0.45 | 0.45 | 0.44 |
| $C_{int}\left(10^4 F\right)$ | 65.0 | 60.0 | 9.0 | 3.0 | 2.8 | 2.2 | 1.8 | 1.6 | 1.9 | 1.8 |
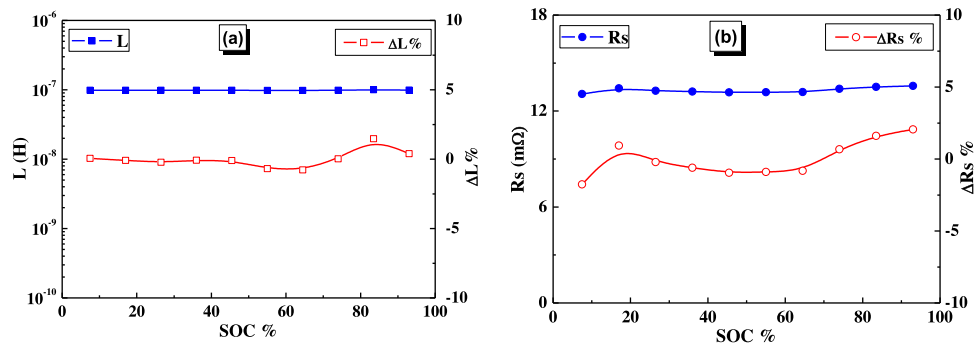


**Fig. 11.** Plots of the inductance and the ohmic resistance from Table 3. (a) Inductance and its relative perturbation with respect to SOC; (b) ohmic resistance and its relative perturbation with respect to SOC.

**Table 4**
Frequency range and the corresponding sub-processes reported in literatures.

| Reference | SEI layer | Charge transfer | Diffusion processes |
|---|---|---|---|
| [42,43] | High frequency | Middle frequency | Low frequency |
| [44][*] | 50k ∼ 5 kHz | 5000 ∼ 10 Hz | 10.0 ∼ 0.0001 Hz |
| [48] | 100k ∼ 10 Hz | 5 ∼ 0.25 Hz | 0.1 ∼ 0.01 Hz |
| [46] | 5000 ∼ 150 Hz | 145 ∼ 0.5 Hz | 0.41-0.005 Hz |
| [50] | 502 ∼ 25.18 Hz | 25.18 ∼ 0.0796 Hz | 0.079 ∼ 0.001 Hz |
| [55] | 350K ∼ 100 Hz | 100 ∼ 1 Hz | 1.0 ∼ 0.003 Hz |

[*] Lithium oxygen battery.

no sharp changes occur in the intrinsic nature of the investigated battery. As a result, characteristic frequencies are valuable indicators to identify different physicochemical processes, and can function as powerful indicators to ascribe specific impedance arcs to certain physicochemical processes [9,28,54].

### 3.5.3. Mapping or assigning

Both characteristic frequency $(f_1, f_2)$ and transition frequency $f_{t2}$ can provide valuable references to assign the separated impedance arcs or tails to corresponding physicochemical processes. In this study, $f_{t1}$ is not adopted because the lower frequency limit of the measurement is much higher than the $f_{t1}$ of the automotive LIB in this study. Fig. 12 shows $f_1$, $f_2$, and $f_{t2}$ evolution trends with respect to SOC for the Li-ion battery. These are basically in agreement with the reported results listed in Table 4. Among $f_1$, $f_2$, and $f_{t2}$, $f_1$ has the weakest dependence of SOC, $f_2$ has the strongest dependence of SOC, and $f_{t2}$ is in the middle. Referring to previous results in Table 4, the identified characteristic frequencies and transition frequencies have greatly facilitated the separation of the processes with overlapping
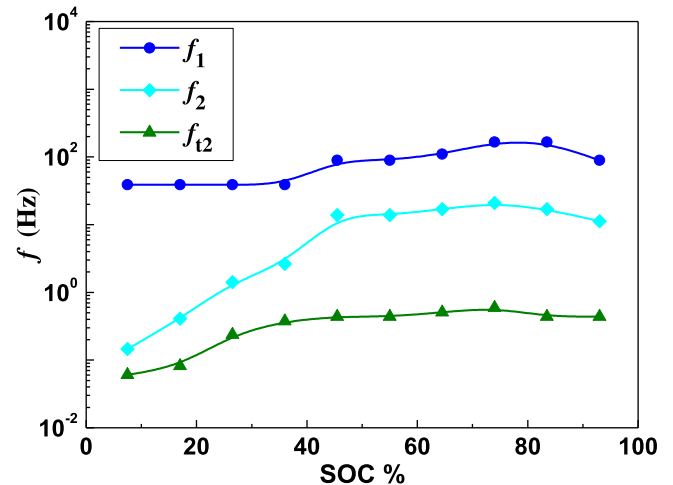


**Fig. 12.** Characteristic frequencies $(f_1, f_2)$ and transition frequencies $(f_{t2})$ evolution trends with respect to SOC for the automotive Li-ion battery.

impedance data, providing more confidence when assigning a specific part of the impedance data (e.g., an impedance arc or loop) to a given physicochemical process as follows: (i) $R_1 \parallel CPE_1$ corresponds to the SEI layer; (ii) $R_2 \parallel CPE_2$ correspond to the charge transfer reaction; and (iii) $Z_{W\infty}$ corresponding to the lithium diffusion behavior. Only when the successful assignment of the fitted circuit parameters to the certain physicochemical processes have been carried out can we analyze and interpret the collected impedance spectra for the automotive LIB.

### 3.6. Analyzing the fractional impedance spectra

Based on the assignments discussed above, three important factors such as the SEI layer status, the charge transfer reaction and the diffusion behavior are analyzed with respect to SOC for the automotive LIB in this study. These factors are necessary for battery management systems, such as in the instances of SOC estimations and state of health predictions in electric vehicles.

#### 3.6.1. Capacitance and fractional exponent

Fig. 13 shows the equivalent capacitances $C_1$ and $C_2$, the fractional exponents $\alpha_1$ and $\alpha_2$, and the intercalation capacitance $C_{int}$. It can be seen that the equivalent capacitance $C_1$ related to the SEI layer is almost independence of SOC, similar to that of the characteristic frequency $f_1$. Meanwhile, the equivalent capacitance $C_2$ related to the charge transfer reaction experiences sharp changes at SOC values between 36.0% and 45.5%. Different from $C_1$ and $C_2$, the interaction capacitance $C_{int}$ steadily decreases with increasing SOC values and a sharp change occurs at a SOC of 17.0%. In addition, $\alpha_1$ has a sharp increase and becomes almost close to 1.0 at SOC values between 36.0% and 45.5%. This sharp change is similar to and coupled with $C_1$. On the contrary, $\alpha_2$ keeps almost constant and is very close to 0.6, which is much lower than $\alpha_1$, suggesting that the interface of the Faradaic charge transfer reaction deviates further from the ideal one than the interface of the SEI layer/electrolyte does.

#### 3.6.2. Polarization loss analysis

Fig. 14 shows the polarization resistances at various SOC values from 7.5% to 93.0% for the automotive LIB. Three conclusions can be drawn from Fig. 14: (i) over the whole SOC range of 7.5% ∼ 93.0%, if maxima/minima of the polarization or diffusion resistances are defined as $r_x \triangleq max/min$, $R_1$ has the smallest $r_{R1} \approx 2.5$, Warburg coefficient $\sigma$ has the largest $r_{Zw} \approx 9.0$, and $R_2$ is in the middle $r_{R2} \approx 4.5$. The larger the ratio of $r_x (x = R_1, R_2, or Z_w)$ is, the larger the SOC effect on polarization loss. This conclusion is not only consistent with previous reports [35,36] but also offers a deep insight into the understanding of different kinds of polarization losses at various SOC values; (ii) neither $R_1$ nor $R_2$ is a monotonical function of SOC, suggesting that both the lithium transfer through SEI layer and the lithium insertion into electrodes has a complex relationship with SOC; (iii) in regard to the distribution of $R_2$ and $\sigma$, there are two domains depending on the level of pre-intercalation: when SOC $\leq$ 26.5%, both $R_2$ and $\sigma$ increase dramatically with decreasing SOC, above this 26.5%, they stayed approximately constant or perturbed only slightly, leading to a constant total polarization resistance $R_p$. Therefore, from the viewpoint of optimal operating range, the automotive LIB should not be operated at high depth of discharge, for example SOC $\leq$ 20%orDOD $\geq$ 80.0%. These diagnosis results indirectly manifest in a degradation mechanism on how DOD can affect the cycling life of the LIB [33]; and (vi) when SOC $\geq$ 26.5%, the resistance of the ohmic resistance $R_s$ is much larger than that of the total polarization resistance $R_p$; when SOC $\leq$ 26.5%, $R_s$ is comparable with $R_p$. This is one obvious difference between a high-power LIB and a normal LIB.

#### 3.6.3. Diffusion behavior evaluation

Rate capabilities of Li-ion batteries rely on both activation polarization and concentration polarization. For the purpose of understanding the limitations of high rate capabilities, it is necessary to evaluate the diffusion coefficient of lithium in porous electrodes filled with liquid electrolyte. Fig. 14d provides a description of the lithium diffusion behavior (herein Warburg coefficient $\sigma$) at various SOC values from 7.5% to 93.0%. In this study, AC impedance was measured with a two-electrode configuration; therefore, the fitted Warburg impedance contains contributions from the electrodes of both the NCM (Li(Ni$_{1/3}$Mn$_{1/3}$Co$_{1/3}$)O$_2$) and the graphite [6,31].

The parameters for the automotive LIB in this study were directly adopted from or indirectly calculated based on the manufacture datasheet: (i) thickness: $l_p = 6.4 * 10^{-5} m$ for the cathode (NCM), $l_n = 7.0 * 10^{-5} m$ for the anode (graphite); (ii) weight: 87.21g for the cathode, 47.89g for the anode; (iii) specific surface area: 0.34m$^2$/g for the cathode, 1.10m$^2$/g for the anode; (iv) interfacial surface of the electrode/electrolyte: $A_p = 29.65$m$^2$ at the cathode/electrolyte, $A_n = 52.68$m$^2$ at the anode/electrolyte interface; and (v) maximum lithium concentration: $C_{p,max} = 0.0477$mol/cm$^3$ in the cathode, $C_{n,max} = 0.0306$mol/cm$^3$ in the anode.

For the convenience of discussion below, $D_p$ and $D_n$ are defined as the lithium diffusion coefficients in the cathode and the anode, respectively, $Z_{W\infty,P}$ and $Z_{W\infty,n}$ are respectively defined as the Warburg impedances of the cathode and the anode, $\sigma_p$ and $\sigma_n$ are respectively defined as the Warburg factors of the cathode (positive electrode) and the anode (negative electrode). With this, we can obtain:

$$C_p = C_{p,max} * (1 - SOC) \tag{9.1}$$

$$C_{p,max} = 0.0495 \quad mol/cm^3 \tag{9.2}$$

$$C_n = C_{n,max} * SOC \tag{9.3}$$

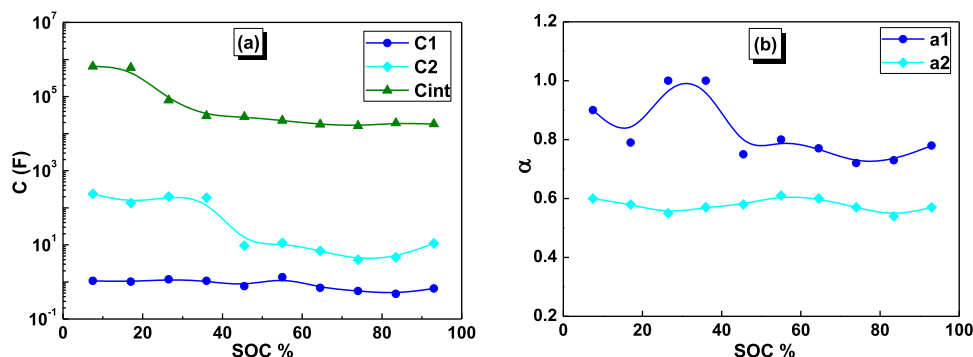$$C_{n,max} = 0.0309 \quad mol/cm^3 \tag{9.4}$$



**Fig. 13.** Equivalent capacitances and intercalation capacitances with respect to SOC values from 7.5% to 93.0% for the automotive LIB.
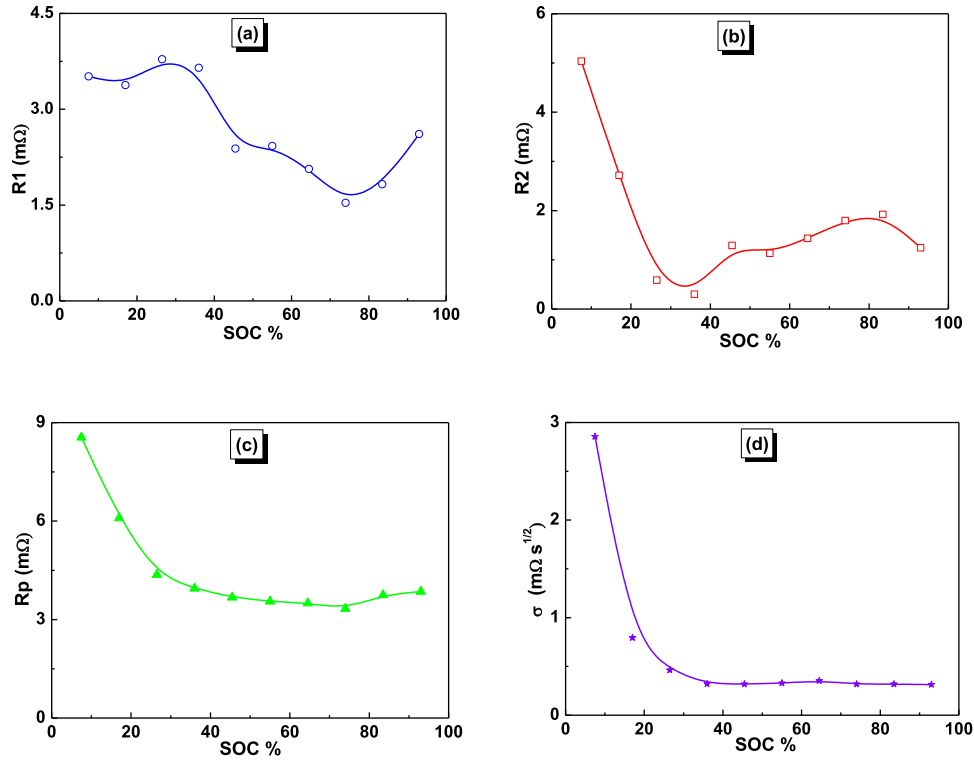
**Fig. 14.** Polarization resistances and Warburg coefficients for the automotive LIB at SOCs from 7.5% to 93.0%. (a) $R_1$, related to SEI layer; (b) $R_2$, related to charge transfer reaction; (c) $R_p \triangleq R_1 + R_2$; (d) Warburg coefficient $\sigma$.

and,

$$\sigma_p = \frac{RT}{n^2 F^2 A_p \sqrt{2} \sqrt{D_p} C_p} \qquad (10.1)$$

$$A_p = 29.65 \ \ m^2 \qquad (10.2)$$

$$\sigma_n = \frac{RT}{n^2 F^2 A_n \sqrt{2} \sqrt{D_n} C_n} \qquad (10.3)$$

$$A_p = 29.65 \ m^2 \qquad (10.4)$$

$$\sigma \triangleq \sigma_p + \sigma_n \qquad (10.5)$$

and,

$$Z_{w\infty,p} = \frac{\sqrt{2}\sigma_p}{\sqrt{j\omega}} \qquad (11.1)$$

$$Z_{w\infty,n} = \frac{\sqrt{2}\sigma_n}{\sqrt{j\omega}} \qquad (11.2)$$

$$Z_{w\infty} \triangleq Z_{w\infty,p} + Z_{w\infty,n} \qquad (11.3)$$

If we further define the Warburg impedance percentage of the electrode relative to the total Warburg impedance,

$$Z_{w\infty,p}\% \triangleq \frac{Z_{w\infty,p}}{Z_{w\infty}} * 100\% \qquad (12.1)$$

$$Z_{w\infty,n}\% \triangleq \frac{Z_{w\infty,n}}{Z_{w\infty}} * 100\% \qquad (12.2)$$

Substituting Eq. (9) ∼ Eq. (11) to Eq. (12) yields,

$$Z_{w\infty,p}\% = \frac{A_n \sqrt{D_n} C_{n,max} SOC}{A_p \sqrt{D_p} C_{p,max}(1 - SOC) + A_n \sqrt{D_n} C_{n,max} SOC} \qquad (12.3)$$

**Table 5**
Diffusion coefficients for graphite and NMC reported in literatures.

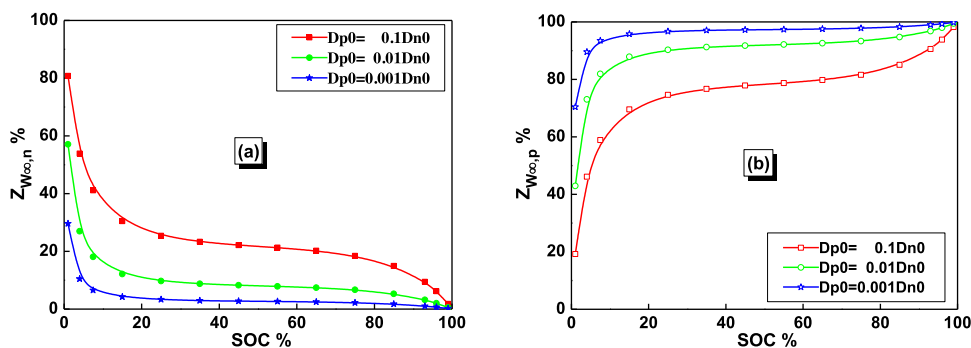| Material | Diffusion Coefficient ($cm^2/s$) | SOC Range | Temperature (°C) | Source |
|---|---|---|---|---|
| **Graphite** | $9.7 * 10^{-13} \sim 2.3 * 10^{-13}$ | 0% ∼ 35.0% | 55 | [56] |
| | $3.2 * 10^{-9} \sim 3.2 * 10^{-12}$ | 10% ∼ 100% | Not given | [46] |
| | $1.1 * 10^{-9} \sim 2.3 * 10^{-11}$ | 0% ∼ 100% | 25 | [57] |
| **NMC** | $9.1 * 10^{-17} \sim 2.4 * 10^{-13}$ | 0% ∼ 100% | 25 | [47] |
| | $1.0 * 10^{-12} \sim 1.0 * 10^{-10}$ | 0% ∼ 100% | Not given | [33] |
| | $3.6 * 10^{-12}$ | Not given | Not given | [52] |

**Fig. 15.** Calculated results of Warburg impedance percentage for both anode and cathode with respect to SOC values from 1.0% to 99.0%. (a) $Z_{w\infty,n}\%$, and (b) $Z_{w\infty,p}\%$ at three different cases of $D_{p0} = 0.1D_{n0}$, $D_{p0} = 0.01D_{n0}$, and $D_{p0} = 0.001D_{n0}$. Herein, $A_p = 29.65m^2$, $A_n = 52.68m^2$, $C_{p,max} = 0.0477mol/cm^3$, $C_{n,max} = 0.0306mol/cm^3$.

$$Z_{w\infty,n}\% = \frac{A_P \sqrt{D_p} C_{p,max}(1 - SOC)}{A_p \sqrt{D_p} C_{p,max}(1 - SOC) + A_n \sqrt{D_n} C_{n,max} SOC} \quad (12.4)$$

In regard to Eq. (12.3) and Eq. (12.4), on one hand, the parameter values of $A_p, A_n, C_{p,max}, C_{n,max}$ and SOC are all given in this study; on the other hand, diffusion coefficients like $D_p$ and $D_n$ are concentration dependent. Two important facts about diffusion coefficients are: (i) diffusion coefficients increases with the increasing availability of lattices in the oxidant, i.e. $D_p$ increases with increasing SOC values, while $D_n$ decreases with increasing SOC values; (ii) in terms of the reported experimental results listed in Table 5, $D_p$ is usually smaller than $D_n$.

In order to simulate $Z_{w\infty}\%$ and $Z_{w\infty,n}\%$ with respect to SOC; similar to the previous method [57], we simplified $D_P$ and $D_n$ relations with $C_p$ and $C_n$ into Eq. (13.1) and Eq. (13.2), respectively,

$$D_p = D_{p0} * (0.5 + SOC)^{3.5} \quad (13.1)$$

$$D_n = D_{n0} * (1.5 - SOC)^{3.5} \quad (13.2)$$

where $D_{p0}$ and $D_{n0}$ are the pre-factors for the cathode diffusion coefficient $D_p$ and the anode diffusion coefficients $D_n$, respectively. At three different cases of $D_{p0} = 0.1D_{n0}$, $D_{p0} = 0.01D_{n0}$, $D_{p0} = 0.001D_{n0}$, we calculated $Z_{w\infty}\%$ and $Z_{w\infty,n}\%$ with respect to SOC based on Eq. (12.1) and Eq. (12.2). The calculating results are plotted in Fig. 15, herein, SOC = 1.0%, 4.0%, 7.5%, 15.0%, 25.0%, 35.0%, 45.0%, 55.0%, 65.0%, 75.0%, 85.0%, 93.0%, 96.0%, and 99.0%. It is clear that when SOC > 25.0%, the cathode becomes the main contributor to $Z_{w\infty}$. Moreover, when the battery enters into the very end stage of charging, i.e. $SOC \to 100\%$ or $C_p \to 0$, $Z_{w\infty,n}$ can be ignored among $Z_{w\infty}$, i.e. $Z_{w\infty,p} \approx Z_{w\infty}$ or $Z_{w\infty,p}\% \to 100\%$.

According to the simulated results in Fig. 15, we can approximate the measured Warburg impedance $Z_{w\infty}$ at the very end stage of charging to the cathode Warburg impedance $Z_{W\infty,p}$. With this, the lithium diffusion coefficient in the cathode can be calculated via Eq. (9)~Eq. (11), i.e. $D_p = 1.9 * 10^{-13} cm^2/s$ at SOC= 93.0%. So, we can obtain $D_{p0}$ according to Eq. (13.1) and in turn, $D_p$ at different SOC values can also be calculated. The estimated results for the cathode Li$^+$ diffusion coefficient of the battery is in a reasonable range [33,47,52]. As demonstrated by Ceder et al. [58], lithium diffusion in bulk is much slower than in nano-particles. Therefore, aside from lithium concentrations, both electrode thicknesses and particle diameters are also important factors affecting lithium diffusion coefficients. In addition, the over or under-estimated interfacial areas of the electrode/electrolyte may also lead to a deviation of the calculated diffusion coefficient.

In summary, it is difficult to measure lithium diffusion coefficients with consistent precision due to the calculated diffusion coefficient being dependent on lithium concentrations, electrode thicknesses, particle diameters, the interfacial area of electrodes/electrolytes, and other operating conditions.

## 4. Conclusions

In this study, a fractional impedance diagnosis was conducted on a commercial NCM/graphite LIB with a rated capacity of 15.4 Ah at various SOC values in an attempt to investigate diffusion behaviors, charge transfer reactions, and SEI layer statuses. The following achievements or conclusions are obtained: first, an impedance diagnosis flowchart is modified by adding two-level feedback loops to the five core steps of measuring, modeling, separating, assigning, and analyzing. With this modified flowchart, conflicts and ambiguities in the understanding of the collected impedance spectra are clarified. Second, a fractional impedance model with consideration for non-ideal interfacials, semi-infinite diffusions, and Li-ion accumulation effects in electrodes is constructed in order to gain deeper insight into the limitations of the rate capabilities of automotive Li-ion batteries. A refinement in the separating or fitting is achieved between the collected impedance data and the constructed circuit model at various SOC values from 7.5% to 93.0%. Third, assisted by characteristic frequencies ($f_1, f_2$) and transition frequencies ($f_{t2}$), the separated impedance arc or tail is assigned and analyzed based on the constructed fractional impedance model with more confidence. Analytical results show that when SOC $\leq 26.5\%$, both the charge transfer resistance $R_2$ and the diffusion impedance $Z_{w\infty}$ increased dramatically with decreasing SOC values, suggesting that automotive Li-ion batteries for electric vehicles should work in DOD below 80%. Fourth, via calculations and simulations for both the anode and the cathode, the Warburg impedance percentages offer a simple and quick way to evaluate lithium diffusion abilities via a two-electrode configuration. The principle method for impedance diagnosis developed in this work also offers a general approach to the investigation of kinetics and dynamics for other energy conversion and storage devices.

# References

[1] P. Miller, State of the art and future developments in lithium-ion battery packs for passenger car applications, Johnson Matthey Technol. Rev. 59 (2015) 4.

[2] L. Lu, X. Han, J. Li, J. Hua, M. Ouyang, A review on the key issues for lithium-ion battery management in electric vehicles, J. Power Sources 226 (2013) 272.

[3] M. Park, X. Zhang, M. Chung, G.B. Less, A.M. Sastry, A review of conduction phenomena in Li-ion batteries, J. Power Sources 195 (2010) 7904.

[4] Y. Xing, E.W.M. Ma, K.L. Tsui, M. Pecht, Battery management systems in electric and hybrid vehicles, Energies 4 (2011) 1840.

[5] L. Zhang, X.S. Hu, Z.P. Wang, F.C. Sun, D.G. Dorrell, Experimental impedance investigation of an ultracapacitor at different conditions for electric vehicle applications, J. Power Sources 287 (2015) 129.

[6] T. Osaka, D. Mukoyama, H. Nara, Review—development of diagnostic process for commercially available batteries, especially lithium ion battery, by electrochemical impedance spectroscopy, J. Electrochem. Soc. 162 (14) (2015) A2529.

[7] Q.A. Huang, R. Hui, B. Wang, J.J. Zhang, A review of AC impedance modeling and validation in SOFC diagnosis, Electrochim. Acta 52 (2007) 8144.

[8] S. Buller, M. Thele, R. Doncker, E. Karden, Impedance-based simulation models of supercapacitors and Li-ion batteries for power electronic applications, IEEE Trans. Ind. Appl. 41 (3) (2005) 742.

[9] J.R. Macdonald, Impedance Spectroscopy—Theory Experiment and Application, John Wiley & Sons, New York, 2005.

[10] M.G.S.R. Thomas, P.G. Bruce, J.B. Goodenough, AC impedance analysis of polycrystalline insertion electrodes: application to $Li_{1-x}Co0_2$, J. Electrochem. Soc. 127 (2) (1985) 1521.

[11] C. Ho, I.D. Raistrick, R.A. Huggins, Application of A-C techniques to the study of Lithium diffusion in tungsten trioxide thin films, J. Electrochem. Soc. 127 (2) (1980) 343.

[12] M.D. Levi, G. Salitra, B. Markovsky, et al., Solid-state electrochemical kinetics of Li-ion intercalation into $Li_{1-x}CoO_2$: simultaneous application of electroanalytical techniques SSCV, PITT, and EIS, J. Electrochem. Soc. 146 (1999) 1279.

[13] K. Takeno, M. Ichimura, K. Takano, J. Yamaki, S. Okada, Quick testing of batteries in lithium-ion battery packs with impedance-measuring technology, J. Power Sources 128 (2004) 67.

[14] W. Waag, S. Käbitz, D.U. Sauer, Experimental investigation of the lithium-ion battery impedance characteristic at various conditions and aging states and its influence on the application, Appl. Energ. 102 (2013) 885.

[15] S.S. Zhang, K. Xu, T.R. Jow, EIS study on the formation of solid electrolyte interface in Li-ion battery, Electrochim. Acta 51 (2006) 1636.

[16] T. Osaka, T. Momma, D. Mukoyama, H. Nara, Proposal of novel equivalent circuit for electrochemical impedance analysis of commercially available lithium ion battery, J. Power Sources 205 (2012) 483.

[17] R. De Revie, The influence of surface roughness of solid elelctrodes on electrochemical measurement, Electrochim. Acta 10 (1965) 113.

[18] P. Mauracher, E. Karden, Dynamic modelling of lead/acid batteries using impedance spectroscopy for parameter identification, J. Power Sources 67 (1997) 69.

[19] L. Gagneur, A.L. Driemeyer-Franco, C. Forgez, G. Friedrich, Modeling of the diffusion phenomenon in a lithium-ion cell using frequency or time domain identification, Microelectron. Reliab. 53 (2013) 784.

[20] L. Zhang, X.S. Hu, Z.P. Wang, F.C. Sun, D.G. Dorrell, Fractional-order modeling and State-of-Charge estimation for ultracapacitors, J. Power Sources 314 (2016) 28.

[21] A.J. Bard, L.R. Faulkner, Electrochemical Methods: Fundamentals and Applications, Second Edition, Wiley, New York, 2001.

[22] C.H. Kim, S. I1. Pyun, J.H. Kim, An investigation of the capacitance dispersion on the fractal carbon electrode with edge and basal orientations, Electrochim. Acta 48 (2003) 3455.

[23] C.A. Schiller, W. Strunz, The evaluation of experimental dielectric data of barrier coatings by means of different models, Electrochim. Acta 46 (2001) 3619.

[24] J.B. Jorcin, M.E. Orazem, N. Pébère, B. Tribollet, CPE analysis by local electrochemical impedance spectroscopy, Electrochim. Acta 51 (2006) 1473.

[25] J. Huang, Z. Li, J.B. Zhang, S.L. Song, Z.L. Lou, N.N. Wu, An analytical three-scale impedance model for porous electrode with agglomerates in Lithium-ion batteries, J. Electrochem. Soc. 162 (4) (2015) A585.

[26] J.Y. Song, M.Z. Bazant, Effects of nanoparticle geometry and size distribution on diffusion impedance of battery electrodes, J. Electrochem. Soc. 160 (1) (2013) A15.

[27] T.B. Hunter, P.S. Tyler, W.S. Smyrl, H.S. White, Impedance Analysis of Poly (vinylferrocene) Films, J. Electrochem. Soc. 134 (1987) 2198.

[28] Q.A. Huang, M.F. Liu, M.L. Liu, Impedance spectroscopy study of an SDC-based SOFC with high open circuit voltage, Electrochim. Acta 177 (2015) 227.

[29] R. Cabanel, G. Barral, J.P. Diard, B. Le Gorrec, C. Montella, Determination of the diffusion coefficient of an inserted species by impedance spectroscopy: application to the $H/H_xNb_2O_5$ system, J. Appl. Electrochem. 23 (1993) 93.

[30] Q.A. Huang, S.M. Park, Unified Model for Transient Faradaic Impedance Spectroscopy: Theory and Prediction, J. Phys. Chem. C 116 (2012) 16939.

[31] A. Ramamurthy, S. Notani, S. Bhattacharya, Advanced lithium ion battery modeling and power stage integration technique, IEEE Energy Conversion Congress and Exposition (ECCE 2010), 12–16 Sept., 2010, pp. 1485.

[32] D.Y. Qu, Application of a.c. impedance technique to the study of the proton diffusion process in the porous $MnO_2$ electrode, Electrochim. Acta 481 (2003) 1675.

[33] S.L. Wu, W. Zhang, X. Song, A.K. Shukla, G. Liu, V. Battaglia, et al., High rate capability of $Li(Ni_{1/3}Mn_{1/3}Co_{1/3})O_2$ electrode for Li-ion batteries, J. Electrochem. Soc. 159 (2012) A438.

[34] L. Lam, P. Bauer, Practical capacity fading model for Li-ion battery cells in electric vehicles, IEEE Trans. Power Electron. 28 (2013) 5910.

[35] E. Barsoukov, J.H. Kim, C.O. Yoon, H. Lee, Universal battery parameterization to yield a non-linear equivalent circuit valid for battery simulation at arbitrary load, J. Power Sources 83 (1999) 61.

[36] R. Ruffo, S.S. Hong, C.K. Chan, R.A. Huggins, Y. Cui, Impedance analysis of silicon nanowire Lithium ion battery anodes, J. Phys. Chem. C 113 (2009) 11390.

[37] D. Andre, M. Meiler, K. Steiner, Ch. Wimmer, T. Soczka-Guth, D.U. Sauer, Characterization of high-power lithium-ion batteries by electrochemical impedance spectroscopy. I. Experimental investigation, J. Power Sources 196 (2011) 5334.

[38] D. Andre, M. Meiler, K. Steiner, Ch. Wimmer, T. Soczka-Guth, D.U. Sauer, Characterization of high-power lithium-ion batteries by electrochemicalimpedance spectroscopy. II: Modelling, J. Power Sources 196 (2011) 5349.

[39] M.E. Orazem, B. Tribollet, An integrated approach to electrochemical impedance spectroscopy, Electrochim. Acta 53 (2008) 7360.

[40] B.A. Boukamp, A nonlinear least squares fit prodecure for analysis of immittance data of electrochemical systems, Solid State Ionics 20 (1986) 31.

[41] H. Xia, L. Lu, G. Ceder, Li diffusion in $LiCoO_2$ thin films prepared by pulsed laser deposition, J. Power Sources 159 (2006) 1422.

[42] S.S. Zhang, K. Xu, T.R. Jow, Electrochemical impedance study on the low temperature of Li-ion batteries, Electrochim. Acta 49 (2004) 1057.

[43] B.L. He, B. Dong, H.L. Li, Preparation and electrochemical properties of Ag-modified TiO2 nanotube anode material for lithium–ion battery, Electrochem. Commun. 9 (2007) 425.

[44] M. Mirzaeian, P.J. Hall, Characterizing capacity loss of lithium oxygen batteries by impedance spectroscopy, J. Power Sources 195 (2010) 6817.

[45] Y.C. Zhang, C.Y. Wang, Cycle-life characterization of automotive Lithium-ion batteries with $LiNiO_2$ cathode, J. Electrochem. Soc. 156 (7) (2009) A527.

[46] T.H. Piao, S.M. Park, C.H. Doh, S.I. Moon, Intercalation of Lithium Ions into Graphite Electrodes Studied by AC Impedance Measurements, J. Electrochem. Soc. 146 (8) (1999) 2794.

[47] L. Wang, J.S. Zhao, X.M. He, J. Gao, J.J. Li, C.R. Wan, C.Y. Jiang, Electrochemical impedance spectroscopy (EIS) study of $LiNi_{1/3}Co_{1/3}Mn_{1/3}O_2$ for Li-ion Batteries, Int. J. Electrochem. Sci. 7 (2012) 345.

[48] Y.L. Cheah, N. Gupta, S.S. Pramana, V. Aravindan, G. Wee, M. Srinivasan, Morphology, structure and electrochemical properties of single phase electrospun vanadium pentoxide nanofibers for lithium ion batteries, J. Power Sources 196 (2011) 6465.

[49] M.E. Levi, Z. Liu, D. Aurbach, Application of finite-diffusion models for the interpretation of chronoamperometric and electrochemical impedance responses of thin lithium insertion $V_2O_5$ electrodes, Solid State Ionics 143 (2001) 309.

[50] P.L. Moss, G. Au, E.J. Plichta, J.P. Zheng, An electrical circuit for modeling the dynamic response of Li-ion polymer batteries, J. Electrochem. Soc. 155 (2008) A986.

[51] J.S. Huang, L. Yang, K.Y. Liu, Y.F. Tang, Synthesis and characterization of $Li3V_{(2-2x/3)}Mg_x(PO_4)_3/C$ cathode material for lithium-ion batteries, J. Power Sources 195 (2010) 5013.

[52] P. Gao, Y. Li, H. Liu, J. Pinto, X. Jiang, G. Yang, Improved high rate capacity and Lithium diffusion ability of $LiNi_{1/3}Co_{1/3}Mn_{1/3}O_2$ with Ordered Crystal Structure, J. Electrochem. Soc. 159 (2012) A506.

[53] M.E. Orazem, I. Frateur, B. Tribollet, V. Vivier, S. Marcelin, N. Pebere, et al., Dielectric properties of materials showing constant-phase-element (CPE) impedance response, J. Electrochem. Soc. 160 (6) (2013) C215.

[54] J.M. Atebamba, J. Moskon, S. Pejovnik, M. Gaberscek, On the interpretation of measured impedance spectra of insertion cathodes for Lithium-ion batteries, J. Electrochem. Soc. 157 (11) (2010) A1218.

[55] K.M. Shaju, G.V.S. Rao, B.V.R. Chowdari, EIS and GITT studies on oxide cathodes, $O^{2-}Li_{(2/3)-x}(Co_{0.15}Mn_{0.85})O_2$ (x = 0 and 1/3), Electrochim. Acta 48 (2003) 2691.

[56] P. Yu, B.N. Popov, J.A. Ritter, R.E. White, Determination of the Lithium ion diffusion coefficient in graphite, J. Electrochem. Soc. 146 (1) (1999) 8.

[57] W.F. Fang, O.J. Kwon, C.Y. Wang, Electrochemical–thermal modeling of automotive Li-ion batteries and experimental validation using a three-electrode cell, Int. J. Energy Res. 34 (2010) 107.

[58] R. Malik, D. Burch, M.Z. Bazant, G. Ceder, Particle size dependence of the ionic diffusivity, Nano Lett. 10 (2010) 4123.